Available online at www.sciencedirect.com
SCIENCE DIRECT
ELSEVIER
European Journal of Mechanics B/Fluids 24 (2005) 255–274
EUROPEAN JOURNAL OF MECHANICS B/FLUIDS

# A Fourier–Boussinesq method for nonlinear water waves

Harry B. Bingham [a,*,1], Yehuda Agnon [b,2]

[a] *Mechanical Engineering, Technical University of Denmark, Lyngby, Denmark*
[b] *Civil Engineering, The Technion, Haifa, Israel*

Received 3 November 2003; received in revised form 10 May 2004; accepted 20 June 2004

Available online 25 September 2004

**Abstract**

A Boussinesq method is derived that is fully dispersive, in the sense that the error of the approximation is small for all $0 \leqslant kh < \infty$ ($k$ the magnitude of the wave number and $h$ the water depth). This is made possible by introducing the generalized (2D) Hilbert transform, which is evaluated using the fast Fourier transform. Variable depth terms are derived both in mild-slope form, and in augmented mild-slope form including all terms that are linear in derivatives of $h$. A spectral solution is used to solve for highly nonlinear steady waves using the new equations, showing that the fully dispersive behavior carries over to nonlinear waves. A finite-difference–FFT implementation of the method is also described and applied to more general problems including Bragg resonant reflection from a rippled bottom, waves passing over a submerged bar, and nonlinear shoaling of a spectrum of waves from deep to shallow water.


*Keywords:* Boussinesq methods; Nonlinear waves; Coastal and offshore engineering; Bragg reflection

## 1. Introduction

Predicting the nonlinear propagation of dispersive waves over a bathymetry is desirable in many coastal and offshore applications. Realistic problems require analysis over a complicated geometry on the order of a hundred by a hundred significant wavelengths, and in relative water depths all the way from practically infinite to zero. Such problems pose a formidable challenge and are generally treated using potential flow methods. Typically the velocity potential is expanded in a set of basis functions which individually satisfy the Laplace equation; and the expansion coefficients are determined to satisfy the remaining conditions on the fluid boundary. The number of degrees of freedom (usually a set of values of the potential or its derivatives on the boundary) is hence significantly smaller than would result from discretizing the entire fluid volume. The basis functions used are typically polynomials, singular Green's functions, or Fourier functions; each of which has advantages and disadvantages depending on the phenomena of primary interest. Boundary integral methods are fully dispersive and simple to apply on complicated geometries, but are relatively computationally demanding since they require discretizing the bottom and lead to full matrix systems. Calculating the Green functions is also more expensive than polynomial or Fourier coefficients. Grilli et al. [1], Wang et al. [2], and Kring et al. [3] are recent examples of the application of boundary element techniques to coastal problems.

* Corresponding author.
*E-mail address:* hbb@mek.dtu.dk (H.B. Bingham).
[1] Supported by the Danish Research Council (STVF) grant no. 9801635, and the Danish Center for Scientific Computing.
[2] Supported by The Fund for the Promotion of Research at the Technion.

0997-7546/$ – see front matter 
doi:10.1016/j.euromechflu.2004.06.006

The pseudo-spectral methods of Liu and Yue [4], and Smith [5] are examples of techniques which are based on Fourier expansions. (Other examples are Craig and Sulem [6], recently extended to 3D by [7], and Clamond and Grue [8]; although these have not yet been applied to variable depth problems.) These methods are also fully dispersive and can be made relatively efficient when combined with a perturbation procedure, but they are more difficult to apply over large depth variations and complicated geometries. Polynomial based methods include Boussinesq methods, many of which are reviewed by [9], Green–Naghdi theory e.g. [10], and the Local Polynomial Approximation (LPA) method of Kennedy and Fenton [11]. Polynomial methods are relatively efficient, since they are formulated on the free-surface boundary alone and lead to sparse algebraic systems, but errors in dispersion eventually become large as the waves become short compared to the water depth. A related approach is the multiterm-coupling technique of [12].

Polynomial methods tend to be preferred for coastal applications as they are relatively easy to implement with good efficiency over complicated geometries with large variations in depth. The trend in these methods over the past several years has been to include higher orders of polynomials and/or more equations in order to extend the range of applicability to larger relative water depths. The high-order Boussinesq method of Madsen, Bingham and Shäffer [13] for example, includes up to fifth-order derivatives and solves three equations at every computational point to extend the range of applicability to $kh \approx 25$. The LPA method achieves a similar accuracy using sixth-order polynomials and solving seven equations ($r = 7$) at every horizontal grid point. These high-order methods involve a substantial increase in complexity relative to low-order Boussinesq methods such as [14], or [15] for example, making them more difficult to implement with $O(N)$ effort ($N$ the number of grid points on the still water plane), and at least an order of magnitude more expensive.

This paper presents a method which is essentially of Boussinesq type but which includes a Generalized Hilbert transform in order to remove any limitation with respect to relative water depth. As the Hilbert transform is evaluated via the Fast Fourier Transform (FFT), this also restricts the computational domain to be a rectangle with periodic (or wall) conditions. At the order chosen for numerical computations, (including up to sixth derivatives) the complexity of the method is comparable to other high-order Boussinesq methods [13] or the LPA method [11] with $r = 7$. In contrast to other polynomial methods however, this Fourier–Boussinesq method approximates the dispersion operator $\tanh(kh)/(kh)$ by a rational function of $kh$ rather than $k^2h^2$ ($k = |\mathbf{k}|$ the magnitude of the wavenumber and $h$ the water depth), and can thus be made asymptotically correct in both limits of $kh$. The Generalized Hilbert operator is then used to convert the odd powers to even powers suitable for evaluation by local finite difference methods. This leads to approximations with small errors in dispersion for all $0 \leqslant kh < \infty$. Here we concentrate on applications in one horizontal dimension, and combine the method with a free-surface perturbation procedure. In this case, a spectral evaluation of the Hilbert operator combined with high-order finite difference evaluation of all derivatives leads to a relatively simple implementation of reasonable accuracy and $O(N \log N)$ computational effort (per time step). Applying the method in two horizontal dimensions and/or avoiding the perturbation procedure is straightforward, but in either case an efficient iterative solver is required to retain the $O(N \log N)$ computational effort. For iterative solutions, it may also be advantageous to evaluate all derivatives spectrally.

The remainder of the paper is organized as follows. In Section 2 we review the exact potential flow problem, and the free-surface perturbation scheme which reduces it to a sequence of linear Laplace problems on a fixed domain bounded by the still water plane. Section 3 derives the Fourier–Boussinesq method for solving this Laplace problem, and derives several variants. Section 4 discusses two techniques for solving non-periodic problems on a periodic domain: relaxation zones; and a decomposition of the potential into periodic and non-periodic components. This includes the necessary extensions to [16] for applying the technique on a variable depth. In Section 5, the practical performance of the model in one horizontal dimension is demonstrated by comparison with analytic and experimental results using both a spectral and a finite-difference–FFT solution. We close with an application of engineering interest which highlights the need to consider a large range of both $k$ and $h$.

## 2. Formulation

We adopt a coordinate system with the $z = 0$ plane at the still water level and the $z$-axis positive upwards, $\mathbf{x} = (x, y)$ is a horizontal vector. The flow is assumed to be irrotational, the fluid incompressible and inviscid, and surface tension is neglected. The fluid volume $\mathcal{V}(\mathbf{x}, z, t)$ is bounded by a free-surface $z = \eta(\mathbf{x}, t)$ and by a bottom $z = -h(\mathbf{x})$. Under the above assumptions the flow can be described by a scalar velocity potential $\phi(\mathbf{x}, z, t)$ which satisfies the following boundary-value problem

$$\nabla^2\phi + \phi_{zz} = 0 \quad \text{in } \mathcal{V}, \tag{1}$$

$$\phi_z + \nabla\phi \cdot \nabla h = 0, \quad z = -h, \tag{2}$$

$$\eta_t + \nabla\tilde{\phi} \cdot \nabla\eta - (1 + \nabla\eta \cdot \nabla\eta)\tilde{\phi}_z = 0, \tag{3}$$

$$\tilde{\phi}_t + \frac{1}{2}\nabla\tilde{\phi} \cdot \nabla\tilde{\phi} - \frac{1}{2}(1 + \nabla\eta \cdot \nabla\eta)\tilde{\phi}_z^2 + g\eta = 0. \tag{4}$$

Here, $\nabla = (\partial/\partial x, \partial/\partial y)$, g is the gravitational acceleration, and partial derivatives are indicated when the independent variables $(\mathbf{x}, z, t)$ appear as subscripts. The free-surface boundary conditions are expressed in terms of the potential at the free-surface $\tilde{\phi} = \phi(\mathbf{x}, \eta(\mathbf{x}, t), t)$ following [17]. Initial conditions on $\eta$ and $\tilde{\phi}$ must also be given.

It is convenient to adopt the perturbation/Taylor series procedure of Dommermuth and Yue [18] for satisfying the free-surface boundary conditions, since this leads to a time-constant $N \times N$ linear system of equations which can be solved using direct matrix methods. In this case, we approximate the potential by a truncated perturbation series in the nonlinearity parameter $\epsilon = ka \ll 1$, where $a$ is a measure of the wave amplitude. Thus $\phi = \sum_{m=1}^{M} \phi^{(m)}$, where $\phi^{(m)} = \mathrm{O}(\epsilon^m)$. The value of $\phi^{(m)}$ on the free surface is then evaluated via a Taylor series expansion from $z = 0$ giving

$$\tilde{\phi} = \sum_{m=1}^{M} \sum_{n=0}^{M-m} \frac{\eta^n}{n!} \frac{\partial^n}{\partial z^n} \hat{\phi}^{(m)}, \tag{5}$$

where $\hat{\phi} = \phi(\mathbf{x}, 0, t)$. Collecting terms at each order of $\epsilon$ provides an explicit sequence for evaluating the potentials:

$$\hat{\phi}^{(1)} = \tilde{\phi}, \tag{6}$$

$$\hat{\phi}^{(m)} = -\sum_{n=1}^{m-1} \frac{\eta^n}{n!} \frac{\partial^n}{\partial z^n} \hat{\phi}^{(m-n)}, \quad m = 2, 3, \ldots, M. \tag{7}$$

Expressed in this form, the problem is reduced to computing $\hat{\phi}_z^{(m)}$ from $\hat{\phi}^{(m)}$, after which further $z$-derivatives are taken by applying the negative horizontal Laplacian to these two quantities. Finally the $z$-derivative of (5) is used to compute $\tilde{\phi}_z$, which allows the free-surface conditions to be stepped forward, closing the problem.

This perturbation procedure implies an assumption of weak nonlinearity, but no restriction on $kh$. The practical limits of the procedure, in combination with the Fourier–Boussinesq method, are considered in Sections 5.1.1 and 5.2.1 where the scheme is shown to converge for nonlinear waves of constant form up to approximately 80% of the stable limiting steepness for any $kh$. This limit is essentially the same as that reported by [18], and although they only considered deep water waves in this context, we have found their method to behave in the same way as ours in shallow water. This is to be expected since our method on a flat bottom, and with the free-surface perturbation scheme, is an approximation to theirs with $\tanh(kh)$ replaced by a rational approximation. We note that these results are not surprising in light of recent work by Nicholls and Reitich [19–21] who have shown that such perturbation schemes (including that of [6]) suffer from cancellation and ill-conditioning which limit their convergence for large perturbations.

We note that it is conceptually straightforward to avoid the perturbation procedure by considering both $\hat{\phi}_z$ and $\hat{\phi}$ as unknowns, as illustrated in Section 3.1. In this case the calculations of Section 5.1 suggest that even steeper waves can be treated, but this has not yet been verified.

## 3. The Fourier–Boussinesq method

As posed above, the problem is solved, given a means of computing the vertical component of velocity at the still water level from the potential at the same level. We derive here a Boussinesq method for this purpose which is asymptotically correct in both limits of $kh$. All existing Boussinesq methods satisfy linear dispersion relations, in terms of non-dimensional wave celerity $c^2/(\mathrm{g}h)$, which are a rational function of $(kh)^2$. This makes them applicable to variable depth problems, since they can be expressed in terms of local differential operators. The exact linear dispersion relation is however transcendental, $c^2/(\mathrm{g}h) = \tanh(kh)/(kh)$, and tends to $1/(kh)$ (an odd power of $kh$) in deep water. Thus, existing Boussinesq methods diverge in this limit. In order to correct the $kh \to \infty$ asymptotics, odd powers of $kh$ are introduced into the approximation, along with the generalized (2D) Hilbert transform operator $\mathcal{H}$ which provides a means of evaluating them in physical space. The generalized Hilbert operator is most conveniently expressed as

$$\mathcal{H}\nabla\phi = \mathcal{F}^{-1}\{k\mathcal{F}\{\phi\}\}, \tag{8}$$

where $\mathcal{F}$ represents the standard 2D ($\mathbf{x} : \mathbf{k}$) Fourier transform and $\mathcal{F}^{-1}$ the inverse transform.

### 3.1. Solutions on a constant depth

Consider first the solution on a constant depth. The starting point for any Boussinesq method is a Taylor series expansion of the velocity potential. Choosing $z = 0$ as the expansion point, and invoking the Laplace equation gives

$$\phi(\mathbf{x}, z, t) = \sum_{n=0}^{\infty} (-1)^n \left( \frac{z^{2n}}{2n!} \nabla^{2n} \hat{\phi} + \frac{z^{2n+1}}{(2n+1)!} \nabla^{2n} \widehat{w} \right), \tag{9}$$

where $\widehat{w} = \phi_z(x, 0, t)$. Inserting (9) into the bottom boundary condition (2) gives

$$\cos(h\nabla)\widehat{w} + \sin(h\nabla) \cdot \hat{\mathbf{u}} = 0, \tag{10}$$

where $\hat{\mathbf{u}} = \nabla\phi(x, 0, t)$, and the sine and cosine Taylor series operators are defined by

$$\begin{aligned} \sin(h\nabla) &= h\nabla - \frac{h^3\nabla^3}{6} + \frac{h^5\nabla^5}{120} + \cdots, \\ \cos(h\nabla) &= 1 - \frac{h^2\nabla^2}{2} + \frac{h^4\nabla^4}{24} + \cdots. \end{aligned} \tag{11}$$

This compact notation is originally due to Rayleigh [22]. Truncating (11) and replacing the continuous gradient operator with a discrete one gives a Taylor Boussinesq method for computing $\widehat{w}$ from $\hat{\mathbf{u}}$. Enhanced methods can be obtained by operating on (10) with another differential operator which converts the Taylor coefficients into Padé coefficients, dramatically improving the performance. Shifting the expansion point down into the fluid as in [13] leads to even more accurate methods, but even these diverge eventually.

Embedded in (10) is the linear dispersion relation. To see this, note that it can be written

$$\widehat{w} = -\tan(h\nabla) \cdot \hat{\mathbf{u}} \tag{12}$$

with the tangent operator defined as the ratio of the operators in (11). In Fourier space (i.e. for a two-dimensional time-harmonic linear solution) $\nabla = \mathrm{i}\mathbf{k}$, $\widehat{w} = (\omega^2/\mathrm{g})\hat{\phi}$, and $\nabla \cdot \hat{\mathbf{u}} = -k^2\hat{\phi}$, where $\omega$ is the radian wave frequency. Plugging these relations into (12) gives $\omega^2 = \mathrm{g}k\tanh(kh)$, the exact linear dispersion relation. Thus the most basic measure of accuracy in dispersion for a Boussinesq method is how well it approximates the linear dispersion operator

$$\frac{c^2}{\mathrm{g}h} = \frac{\tanh(\kappa)}{\kappa}, \tag{13}$$

where $\kappa = kh$ has been introduced for brevity.

Having defined the generalized Hilbert operator as a way of evaluating $k$ in physical-space (as opposed to i**k**), we may now investigate rational approximations to the linear dispersion operator including both even and odd powers of $\kappa$. To illustrate, consider the simplest example: the lowest order rational function of $\kappa$ which has the correct limiting behavior for both $\kappa \to 0$ (long wave limit) and $\kappa \to \infty$ (short wave limit) is

$$\frac{c^2}{\mathrm{g}h} \approx \frac{1}{1+\kappa}. \tag{14}$$

This approximate dispersion relation defines the lowest order Fourier–Boussinesq method. To express the method in **x**-space, use (14) to approximate the tangent operator in (12), then associate i$\kappa$ with $h\nabla$ and $\kappa$ with $h\mathcal{H}\nabla$. Thus

$$\tan(h\nabla) = \mathrm{i}\tanh(\kappa) \approx \frac{\mathrm{i}\kappa}{1+\kappa} = \frac{h\nabla}{1+h\mathcal{H}\nabla}, \tag{15}$$

which gives

$$[1 + h\mathcal{H}\nabla]\widehat{w} = -h\nabla \cdot \hat{\mathbf{u}} \tag{16}$$

as the equation to be solved for $\widehat{w}$. In this form, a fast numerical solution can only be obtained iteratively since the Hilbert operator appears on the left-hand side of the equation, and it's fast evaluation requires an explicit sequence of numerical operations (i.e. FFT$\{\widehat{w}\}$, multiply by $k$, inverse FFT). It turns out that any Fourier–Boussinesq method can be expressed in a form amenable to direct matrix methods by multiplying both numerator and denominator by the denominator with $\kappa$ replaced by $-\kappa$. For example, (15) can be written $\mathrm{i}\tanh(\kappa) \approx \mathrm{i}\kappa(1-\kappa)/(1-\kappa^2) = h\nabla(1-h\mathcal{H}\nabla)/(1+h^2\nabla^2)$, which removes the Hilbert operator from the left-hand side and allows for a direct solution to the linear system. Note however, that this example is only included for illustration purposes as the corresponding numerical method is unstable due to the real root of the denominator, which must be avoided in practice.

Finally, we note that when an iterative solution is to be pursued it may be advantageous to dispense with the free-surface perturbation procedure. This is most easily done by combining a truncated version of (9) applied at $z = \eta$ with the Fourier–Boussinesq approximation to (12). This system of equations is solved to get $\hat{\phi}$ and $\widehat{w}$, after which the $z$-derivative of (9) is used to get $\widetilde{w}$. For example, using the lowest order model we truncate (9) at $n = 0$ and combine it with (16) to get the system

$$\begin{aligned} &\hat{\phi} + \eta\widehat{w} = \tilde{\phi}, \\ &h\nabla^2\hat{\phi} + [1 + h\mathcal{H}\nabla]\widehat{w} = 0, \end{aligned} \tag{17}$$

which when solved provides $\widetilde{w}$ from $\widetilde{w} = \widehat{w} - \eta\nabla^2\hat{\phi}$.

This lowest order method is only of interest for very long or very short waves, of more interest are higher order approximations which are developed in the following.

*3.1.1. Padé based rational approximations*

The idea behind the Fourier–Boussinesq method is to manipulate the rational approximation to the dispersion operator (correct the $\kappa \to \infty$ asymptotics) and obtain a good approximation for all $\kappa$. One way to do this is to find the Padé $(m, n)$ approximation to the function $\tanh(\kappa) - 1$ at the point $\kappa = 0$. Adding one to the result and dividing by $\kappa$ gives the corresponding approximate dispersion operator. As long as $m < n$ the correct asymptotics are obtained in both limits of $\kappa$. Finally, by associating $\kappa$ with $h\mathcal{H}\nabla$ and $\kappa^{2n}$ with $(-\mathrm{i}h\nabla)^{2n}$ (as illustrated above) a method in **x**-space is obtained. Two examples are obtained by using Padé (1,4) and Padé (3,6) approximations in the above procedure to obtain

$$(15 + 9\kappa + 9\kappa^2 + 4\kappa^3 + \kappa^4)\widehat{w} = -(15 + 9\kappa + 4\kappa^2 + \kappa^3)h\nabla\cdot\hat{\mathbf{u}}, \tag{18}$$

and

$$(1890 + 630\kappa + 945\kappa^2 + 285\kappa^3 + 75\kappa^4 + 12\kappa^5 + \kappa^6)\widehat{w} = -(1890 + 630\kappa + 315\kappa^2 + 75\kappa^3 + 12\kappa^4 + \kappa^5)h\nabla\cdot\hat{\mathbf{u}} \tag{19}$$

respectively. We refer to these methods as Padé (3,4) and Padé (5,6) methods, due to the final form of the approximate dispersion operator.

As discussed above, the equations in this form must be implemented iteratively. An iterative solution will be preferred in two horizontal dimensions, and this work is in progress, but a direct implementation is more straightforward, and in one horizontal dimension it is more efficient. For these reasons we now consider alternatives to Padé approximation which lead to slightly different rational approximations, and can be designed for direct matrix methods. We will concentrate on the (5,6) form of the method, as this represents a reasonable balance between overall accuracy and computational complexity.

*3.1.2. Modified rational approximations*

In the previous section we applied the Padé approximation in a special way which introduced odd powers into the approximation of $\tanh(\kappa)/\kappa$, correcting the $\kappa \to \infty$ asymptotics to give a good fit everywhere. Comparing (18) with a direct Padé (5,6) approximation of the dispersion operator, shows that we have sacrificed accuracy near the expansion point ($\kappa = 0$) to obtain a better overall fit. This is a common theme in the practice of rational approximation, and a number of methods exist for finding an approximation based on some definition of goodness of fit over an interval rather than on an expansion about a particular point. Economized rational approximations, rational interpolations, min-max rational approximations, and least-squares fitting are some widely used examples.

As an illustration of a more general approach, consider the rational approximation $p(m)/q(n) \approx f(\kappa)$, where $p$ and $q$ are polynomials in $\kappa$ of degree $m$ and $n$ respectively. Choosing values for $m$ and $n$ with $m < n$, along with $m + n + 1$ points in $\kappa$ at which to enforce the approximation, gives $m + n + 1$ equations for the unknown coefficients of $p$ and $q$. In our case we must restrict the form of the approximation slightly to ensure the correct asymptotics in both limits of $\kappa$ and take

$$\frac{\tanh\kappa}{\kappa} \approx \frac{1 + a_1\kappa + a_2\kappa^2 + a_3\kappa^3 + a_4\kappa^4 + a_5\kappa^5}{1 + b_1\kappa + b_2\kappa^2 + b_3\kappa^3 + b_4\kappa^4 + b_5\kappa^5 + a_5\kappa^6}. \tag{20}$$

Collocating (20) at the Gauss points over the interval $0 \leqslant \kappa \leqslant 6$ for example, gives a modified version of (19) with the coefficients labelled as "modified" in Table 1. The corresponding dispersion errors are shown in Fig. 1 which also includes the errors due to the original Padé based coefficients. It is clear that accuracy has been further sacrificed near $\kappa = 0$ to get much improved overall accuracy. (In this case the maximum errors are of $O(10^{-7})$ for $0 \leqslant \kappa \leqslant 1$). Continuing in this vein, we set $b_1 = b_3 = b_5 = 0$ to obtain a method which is easy to implement using direct matrix methods. Solving for the remaining coefficients gives those labelled as "direct" in Table 1 and the corresponding errors shown in Fig. 1. In this case we have chosen to compute the coefficients based on a least-squares fitting strategy over $0 \leqslant \kappa \leqslant 7$, rather than using simple collocation, although the two give similar results.

Table 1
Modified and direct coefficients in (20) scaled by 1890 for comparison with (19). Corresponding dispersion errors are shown in Fig. 1

| | Modified | Direct | | Modified | Direct |
|---|---|---|---|---|---|
| $a_1$ | 619.336 | 1.69577 | $b_1$ | 619.326 | 0 |
| $a_2$ | 344.442 | 182.429 | $b_2$ | 974.629 | 815.374 |
| $a_3$ | 87.3517 | −0.218759 | $b_3$ | 292.925 | 0 |
| $a_4$ | 16.6195 | 0.946735 | $b_4$ | 91.2142 | 20.566 |
| $a_5$ | 3.08021 | 4.60818 | $b_5$ | 16.5 | 0 |

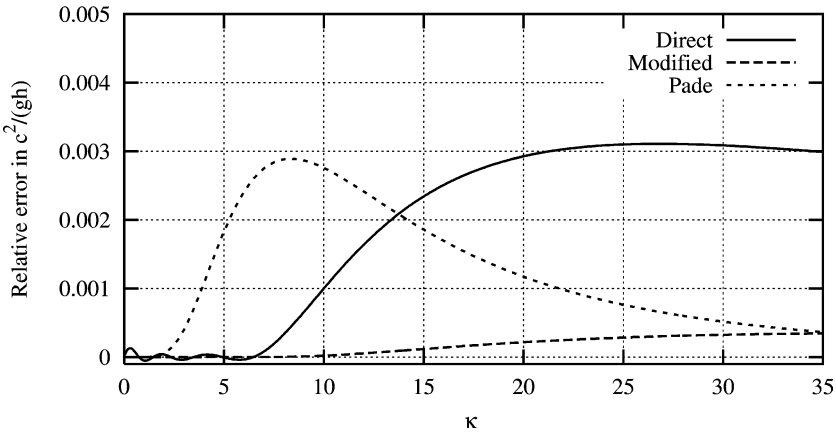


Fig. 1. Relative error in $c^2/(gh)$ using the modified and Direct(5,6) coefficients of Table 1 in (20). Errors using (19) are also shown for reference with label Padé.

### 3.2. Solutions on a sloping bottom

When a variation of the depth is retained in the bottom boundary condition, it takes the form

$$\cos(h\nabla)\widehat{w} + \sin(h\nabla)\cdot\hat{\mathbf{u}} + \nabla h\cdot\left[\cos(h\nabla)\hat{\mathbf{u}} - \sin(h\nabla)\widehat{w}\right] = 0. \tag{21}$$

I.e. (9) inserted into (2), with $h(\mathbf{x})$. For the case of variable depth, the derivation of the approximate equation is more involved. Modifying the sine and cosine operators from their original Taylor series form corresponds to operating on the equation with another differential operator. Since $\nabla$ and $h(\mathbf{x})$ do not commute, this produces new terms involving $\nabla h$, $(\nabla h)^2$, $\nabla^2 h$, etc. It is common practice to neglect terms that are higher than $O(\nabla h)$, which is a mild-slope approximation. In [23] all the terms which are linear in the derivatives of $h$ were retained to get an augmented mild-slope equation. These higher derivative terms play an important role in Bragg resonance and in reflection, so it can be of interest to retain them. In the following sub-sections, we take two approaches to deriving the slope terms for a Boussinesq method. The first approach is to approximate the bottom locally by a sloping plane, and rotate the coordinate system in parallel with the bottom. The second approach is to Taylor expand the bottom boundary condition about a flat bottom. By keeping the linear term in this expansion, all terms which are linear in the derivatives of $h$ are retained, giving an augmented mild-slope approximation. This result can also be reduced to a mild-slope approximation. Only the second approach leads to computationally attractive methods in this context, and the performance of the resulting Direct(5,6) methods is addressed in Section 5.2.

#### 3.2.1. Coordinate transformation approach

Consider the operator

$$(h+z)\nabla_b = (h+z)(\nabla - \nabla h\partial_z), \tag{22}$$

where $\nabla_b$ is the $O(\nabla h)$ approximation to the gradient along a surface parallel to the bottom, and $\partial_z$ is the derivative in the $z$ direction. The operator $\nabla_b$ commutes with $h+z$, just as $\nabla$ commutes with $h$ on a horizontal bottom. It is easily checked that, to order $\nabla h$, higher powers of this operator can be evaluated through

$$\left[(h+z)\nabla_b\right]^n = (h+z)^n\nabla^n - n(\nabla h)(h+z)^n\nabla^{n-1}\partial_z. \tag{23}$$

This expression can be used to write

$$\cos\big((h+z)\nabla_b\big) = \cos\big((h+z)\nabla\big) + (h+z)\sin\big((h+z)\nabla\big)\partial_z, \tag{24}$$

$$\sin\big((h+z)\nabla_b\big) = \sin\big((h+z)\nabla\big) - (h+z)\cos\big((h+z)\nabla\big)\partial_z. \tag{25}$$

In general, any polynomial of the form $A$ in which the argument is replaced by $(h+z)\nabla_b$, can be approximated by

$$A\big((h+z)\nabla_b\big) = A\big((h+z)\nabla\big) - (h+z)A'\big((h+z)\nabla\big)\partial_z, \tag{26}$$

where $A'$ is the derivative of $A$ with respect to its argument. This expression also holds for operators that correspond to odd powers of $k$, since they can be approximated by polynomials in $\nabla^2$ and the Hilbert operator. For example

$$(h+z)^3k_b^3 = (h+z)^3k^3 - (h+z)^3 3k^2\mathcal{H}\nabla\partial_z. \tag{27}$$

Next, approximate (21) by

$$\cos\big((h+z)\nabla_b\big)(\widehat{w}+\nabla h\cdot\hat{\mathbf{u}})+\sin\big((h+z)\nabla_b\big)\cdot(\hat{\mathbf{u}}-\nabla h\widehat{w})=\mathrm{O}\big(\nabla^2 h,(\nabla h)^2\big), \tag{28}$$

which is valid at any level $z$. This can be checked by direct calculation. It expresses the Boussinesq expansion in a coordinate system that is parallel to the bottom.

It is now sufficient to replace $h\nabla$ in the expressions that were obtained in the even depth case by the operator $(h+z)\nabla_b$, and use (23). Setting $z=0$ gives

$$B\widehat{w}+A\hat{\mathbf{u}}=\nabla h\big(A+A'h\nabla\big)\widehat{w}-(B+B'h\nabla)\hat{\mathbf{u}}, \tag{29}$$

where $A/B$ is a rational approximation to the tangent operator, and use was made of the relations $\partial_z\hat{\mathbf{u}}=\nabla\widehat{w}$ and $\partial_z\widehat{w}=-\nabla\cdot\hat{\mathbf{u}}$. To ensure that the $\widehat{w}$ operator is differential, the following operator is applied to (29)

$$B_- - \nabla h(A_- + A'_- h\nabla), \tag{30}$$

where $A_-(kh)=A(-kh)$. Note that the product of two operators can be expanded based on

$$h^n\nabla^n\big(h^m\nabla^m\big)=h^{n+m}\nabla^{n+m}+h(\nabla h)nmh^{n+m-2}\nabla^{n+m-2}+\mathrm{O}\big((\nabla h)^2\big). \tag{31}$$

Thus, for two operators, $G$ and $F$

$$G(h\nabla)F(h\nabla)=G*F(h\nabla)+h(\nabla h)G'*F'(h\nabla)\nabla+\mathrm{O}\big((\nabla h)^2\big), \tag{32}$$

where $G*F$ is the product of the functions $G$ and $F$, and $G'$ and $F'$ their derivatives. The resulting equation

$$\begin{aligned}BB_-\widehat{w}+AB_-\hat{\mathbf{u}}=\nabla h\big(&B_-A+A_-B+(B_-A'+A'_-B-B'A')h\nabla\big)\widehat{w}\\&-\big(B_-B-A_-A+(B_-B-AA'_-+B'B')h\nabla\big)\hat{\mathbf{u}}\end{aligned} \tag{33}$$

has the appropriate form and is equivalent to (29) to order $\nabla^2 h$, $(\nabla h)^2$.

This approach has a few drawbacks. One is that the shoaling performance depends on the accuracy of the approximation for first and second derivatives of the dispersion relation with respect to $\kappa$. These are typically less accurate than the approximate dispersion relation itself, so very high order methods are required. The final form with a purely differential implicit operator then doubles the order of the method. In addition, this approximation introduces errors which are $\mathrm{O}((\nabla h)^2,\nabla^2 h)$, but have large numerical coefficients. Thus the equations in this form are not especially well suited to practical implementation.

*3.2.2. Perturbation approach*

An alternative approach is to introduce a perturbation expansion in the depth deviation $\delta=(h-h_0)/h_0$ from a local reference depth $h_0$, in the manner used by [23] to study the augmented mild-slope equation. This approach greatly simplifies the analysis, since $\nabla$ and $h_0$ commute. By keeping only the linear term in the resulting expansion, all terms that are linear in the derivatives of $h$ are included.

We begin by expanding $\widehat{w}$ as

$$\widehat{w}=\widehat{w}_0+\widehat{w}_1+\mathrm{O}\big(\delta^2\big), \tag{34}$$

where $\widehat{w}_0$ is the solution to the equation

$$B\widehat{w}_0+A\cdot\hat{\mathbf{u}}=0, \tag{35}$$

and $A/B$ represents an approximation to $\tan(h\nabla)$. Expanding the exact bottom condition (21) to $\mathrm{O}(\delta)$, and operating on the result with $\sec(h_0\nabla)$, we get (cf. [23, Eq. (2.9)])

$$\widehat{w}+\tan(h_0\nabla)\cdot\hat{\mathbf{u}}=-\sec(h_0\nabla)h_0\nabla\cdot\big(\delta\sec(h_0\nabla)\hat{\mathbf{u}}\big). \tag{36}$$

Expanding (35) to $\mathrm{O}(\delta)$ about the local reference depth $h_0$ gives

$$B_0\widehat{w}_0+A_0\cdot\hat{\mathbf{u}}+\delta B'h_0\nabla\widehat{w}_0+\delta A'h_0\nabla\cdot\hat{\mathbf{u}}=B_0\widehat{w}_0+A_0\cdot\hat{\mathbf{u}}+\delta(A'-B'B_0^{-1}A_0)h_0\nabla\cdot\hat{\mathbf{u}}=0, \tag{37}$$

where $B_0=B(h_0\nabla)$ and $A'$, $B'$ stands for the derivative of the operator with respect to its argument $(h\nabla)$, and evaluated at $h_0\nabla$. Operating on this equation with $B_0^{-1}$ gives

$$\widehat{w}_0=-B_0^{-1}A_0\cdot\hat{\mathbf{u}}-B_0^{-1}\delta(A'-B'B_0^{-1}A_0)h_0\nabla\cdot\hat{\mathbf{u}}, \tag{38}$$

and since $B_0^{-1}A_0$ is the approximation we use for $\tan(h_0\nabla)$, $\widehat{w}_1$ is given by

$$\widehat{w}_1=\widehat{w}-\widehat{w}_0=-\sec(h_0\nabla)h_0\nabla\cdot\delta\sec(h_0\nabla)\hat{\mathbf{u}}+B_0^{-1}\delta(A'-B'B_0^{-1}A_0)h_0\nabla\cdot\hat{\mathbf{u}}. \tag{39}$$

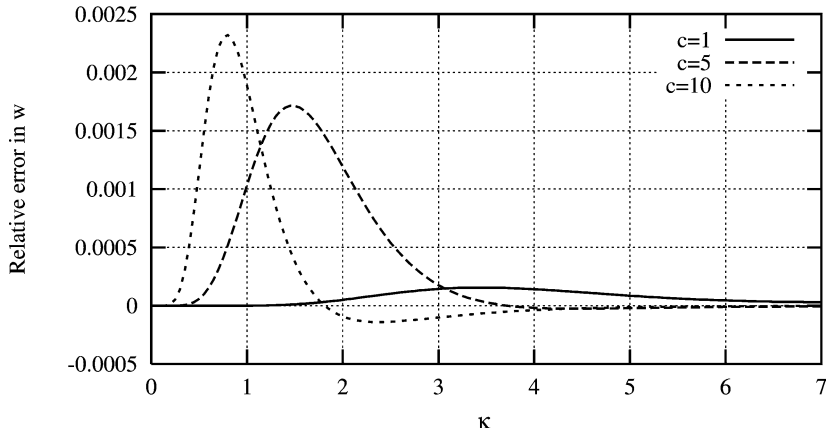


Fig. 2. Relative error in $\widehat{w}$ introduced by using the Padé (4,6) approximation of the operator $\sec(h\nabla)$ in Eq. (39). Different curves are for different bottom slope wave number $K$ relative to the surface wave number $k$ where $K = ck$, with a bottom variation magnitude 20% of the local depth.

This is the augmented mild-slope Fourier–Boussinesq method.

To evaluate (39), we use the fact that an expression of the form $F(h_0\nabla)\delta f$, where $F$ is an operator and $f$ a function, can be evaluated through

$$F(h_0\nabla)\delta f = F(h_0\nabla)\frac{h}{h_0}f - \frac{h}{h_0}F(h_0\nabla)f. \tag{40}$$

The model is thus non-local, $\delta$ is used in the derivation but drops from the final equations. The result is an approximation to the augmented mild-slope equation including all terms which are linear in the derivatives of $h$. For implementation, an approximation to the $\sec(h_0\nabla)$ operator is required. Since this function decays as $\kappa$ increases, a Padé $(m,n)$ approximation with $m < n$ is appropriate. For the Direct(5,6) method, we use a Padé (4,6) approximation

$$\operatorname{sech}(\kappa) \approx \frac{1 - \kappa^2/39 + 17\kappa^4/65520}{1 + 37\kappa^2/78 + 1907\kappa^4/65520 + 59\kappa^6/131040}, \tag{41}$$

which involves only derivatives (no Hilbert transform). The relative errors in the total $\widehat{w}$ introduced by this approximation are shown in Fig. 2. To evaluate the error we have assumed a bottom variation of the form $\delta = d\cos Kx$ with $d = 0.2$ (a very large value) and chosen several values of $K$ relative to the surface wave number $k$.

Eq. (39) can also be conveniently reduced to a mild-slope approximation. Ignoring higher derivative terms simply means that $F(h_0\nabla)\delta f = \nabla h F'(h_0\nabla)f + \mathrm{O}(\nabla^2 h)$, in which case (39) reduces to

$$\widehat{w}_1 = \nabla h \cdot \left[-\sec^2(h_0\nabla)\big(1 + \tan(h_0\nabla)h_0\nabla\big) + \big(B_0^{-1}\big)'(A' - B'B_0^{-1}A_0)h_0\nabla\right]\hat{\mathbf{u}}. \tag{42}$$

Since this operator is a smooth function which decays exponentially with increasing $\kappa$, it is convenient to approximate it by another operator of $(2m, 2n)$ form with $m < n$, which involves only derivatives. Thus, for the Direct(5,6) method we write

$$\widehat{w}_1 \approx -\nabla h \cdot \frac{1 + \alpha_2 h^2\nabla^2 + \alpha_4 h^4\nabla^4}{1 + \beta_2 h^2\nabla^2 + \beta_4 h^4\nabla^4 + \beta_6 h^6\nabla^6}\hat{\mathbf{u}} \tag{43}$$

and make a least squares fit between the two operators over $0 \leqslant \kappa \leqslant 6$. This gives the coefficients in Table 2 and the overall relative error for $\widehat{w}$ (taking $\nabla h = 1$) shown in Fig. 3.

We note that the approach outlined here is valid for any rational approximation to the dispersion operator, and is by no means restricted to Fourier–Boussinesq methods.

## 4. Lateral boundary conditions

Introducing the FFT requires periodic (or symmetric) boundary conditions at the lateral boundaries. The typical method of overcoming this limitation is to successively increase the size of the computational domain until the effect of the boundaries becomes negligible, e.g. [18]. Here we discuss two other approaches for solving non-periodic problems on a periodic computational domain: relaxation zones, and a decomposition of the solution into periodic and non-periodic components. These two techniques, may be used alone or in combination.

Table 2
Coefficients appearing in (43), which approximates (42) for the Direct(5,6) method, to give the errors shown in Fig. 3

| | | | |
|---|---|---|---|
| $\alpha_2$ | $-1.762 \times 10^{-1}$ | $\beta_2$ | $-1.320$ |
| $\alpha_4$ | $-7.759 \times 10^{-3}$ | $\beta_4$ | $6.433 \times 10^{-1}$ |
| | | $\beta_6$ | $-2.141 \times 10^{-1}$ |

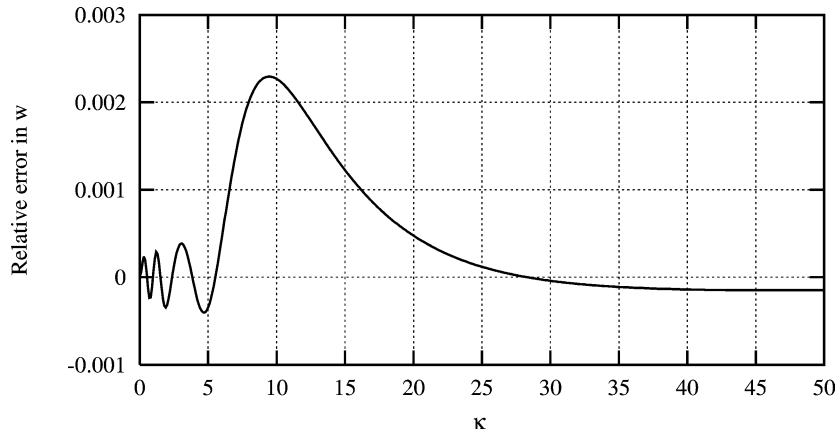


Fig. 3. Relative error in $\widehat{w}$ introduced by approximating the mild-slope correction operator of (42) by the purely differential operator of (43) with the coefficients of Table 2. Shown here for $\nabla h = 1$.

### 4.1. Relaxation zones

When a computational boundary coincides with a physical boundary a physical boundary condition can be applied, but to simulate an unbounded physical domain we require an *artificial* boundary condition. Weakly-reflecting artificial boundary conditions have been the subject of considerable attention over the past 30 years or more, and the topic is reviewed by [24,25] for example. The particular form of artificial boundary condition we apply here is to relax the numerical solution towards a specified analytic solution over a region near the boundary, an idea which is often applied in ocean circulation modelling (see e.g. [26] who modified the idea proposed by [27]). Such a *relaxation zone* for simultaneous generation and absorption of waves is readily achieved by simply defining a relaxation coefficient $0 \leqslant c_r(\mathbf{x}) \leqslant 1$, and an exact desired solution $(\eta^{\mathrm{e}}, \phi^{\mathrm{e}})$. After each stage of the time integration the solution within the relaxation zone is then redefined to be

$$\begin{aligned} \eta(\mathbf{x},t) &= \big[1 - c_r(\mathbf{x})\big]\eta(\mathbf{x},t) + c_r(\mathbf{x})\eta^{\mathrm{e}}(\mathbf{x},t), \\ \phi(\mathbf{x},t) &= \big[1 - c_r(\mathbf{x})\big]\phi(\mathbf{x},t) + c_r(\mathbf{x})\phi^{\mathrm{e}}(\mathbf{x},t). \end{aligned} \tag{44}$$

Experience has shown that a good choice of coefficient is $c_r(\sigma) = (1 - 3/5\sigma)^8$ where $\sigma$ is a scaled coordinate perpendicular to the boundary with $\sigma = 0$ the boundary and $\sigma = 1$ the end of the relaxation zone. The technique is very effective, as is demonstrated by Fig. 4. This shows the steady-state envelope of a calculation using a linear traveling wave as the desired solution in a relaxation zone of one wavelength at the left end of the domain. The right hand boundary is a fully-reflective wall, and the result is a perfect traveling wave at the wave maker, which blends smoothly into a perfect standing wave outside of the relaxation zone. If waves of very different lengths need to be absorbed, it is best to combine this technique with a decomposition of the potential which allows non-periodic conditions (e.g. a time-dependent flux) to be applied at the boundaries, as is discussed in the next section.

### 4.2. Splitting the potential into periodic and non-periodic components

This section describes a method for introducing general conditions at the lateral boundaries of the computational domain. It is an extension to the method of [16] to include a mild-slope bottom. The computational domain $\mathcal{V}$ is enclosed within a

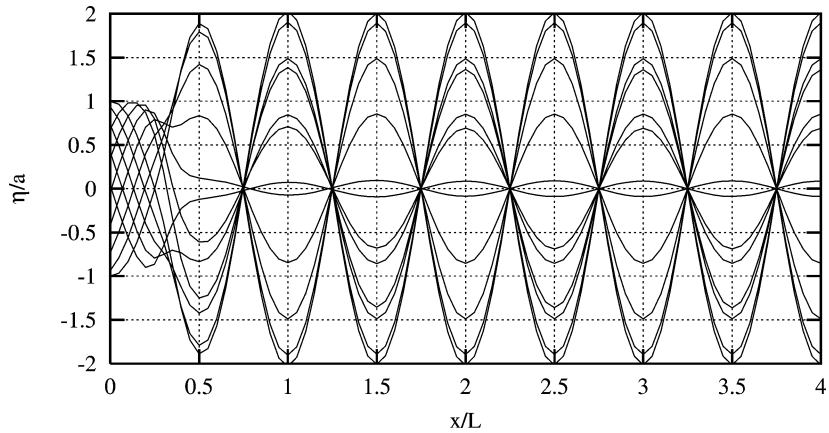


Fig. 4. Demonstration of simultaneous wave generation and absorption from a relaxation zone. A linear incident wave is specified at the left hand boundary using a relaxation zone of one wavelength. The right hand boundary is a wall. The steady-state result is a perfect traveling wave at the wave-maker, and a perfect standing wave outside of the relaxation zone.

set of control surfaces which are taken to be the vertical planes at $x = 0, x = l_x, y = 0,$ and $y = l_y$. On these control surfaces, boundary conditions of the following form are applied

$$u_n = \sum_{j=1}^{N_3} c_j U_j, \tag{45}$$

where $N_3$ is the total number of degrees of freedom distributed over the control surface, $u_n$ is the velocity normal to each control surface, and the $U_j$ are functions of time and of the horizontal coordinate. The $U_j$ can be chosen to represent a wave maker/absorber or a matching to another computational domain. In general $U_j$ may have a vertical structure, which can be included in the solution. However, in many applications there is no interest in resolving this structure, which is essentially responsible for evanescent modes that decay exponentially away from the boundary. For simplicity, we demonstrate the method for $U_j$ that are independent of $z$.

The velocity potential is decomposed into a sum of two potentials,

$$\phi = \phi_1 + \phi_2 \tag{46}$$

$$\phi_2 = \sum_{j=1}^{N_3} c_j \phi_{2j}. \tag{47}$$

The potentials $\phi_{2j}$ are chosen to satisfy the Laplace equation and the bottom boundary conditions (1) and (2); and a set of modal distributions of normal velocity on the control surfaces. It is convenient to take $\phi_2$ to be quadratic in $z$, corresponding to "steady" flow fields, in which case the resultant horizontal velocity is independent of $z$. As an example, take $\phi_{21}$ to be the solution for the two dimensional flow with $u = 0$ on $x = 0, y = 0,$ and $y = l_y$; but $u = U$ at $x = l_x$. This is simply a corner flow, and the solution is

$$\left(\nabla\phi_{21}, \frac{\partial\phi_{21}}{\partial z}\right) = \frac{U}{l_x}\big(x - 2(z+h)h_x, 0, -(z+h+xh_x)\big). \tag{48}$$

This flow satisfies the Laplace equation only at the leading order, with an error which is $O(\nabla^2 h, (\nabla h)^2)$. On an even bottom $\nabla h$ vanishes and the form given by [16] is recovered. Similar solutions can be used for the remaining $\phi_{2j}$ corresponding to constant flows through the other three vertical control boundaries. If $U$ has spatial structure over the control surface (or if we wish to have a solution which is accurate to any order in the bottom slope), $\phi_2$ can be pre-solved for a full basis set of lateral boundary conditions, producing a set of time-independent response functions (or a single such function) which may then be used in the solution, at each time step.

Having chosen the appropriate form of (45) to ensure the generation and/or absorption of waves for example, the other part of the potential, $\phi_1$, represents (mathematically) a flow in a closed basin. The complete potential $\phi = \phi_1 + \phi_2$ must finally satisfy the remaining boundary conditions on the free-surface, (3). Thus we proceed as follows: Given $\tilde{\phi}$ and $\eta$, $\phi_2$ is determined from the lateral boundary condition (45) using the pre-solved steady flows. This gives $\tilde{\phi}_1$ from which $\tilde{\phi}_{1z}$ is computed using one of

the above described Fourier–Boussinesq methods. Together with the horizontal gradient of $\phi$ and $\eta$, this provides all the terms appearing in the free-surface boundary conditions, which are finally marched in time to get the new values of $\tilde{\phi}$ and $\eta$.

## 5. Calculations

The linear dispersion and shoaling properties of the method were established in Section 3, here we provide numerical calculations which establish the nonlinear properties. Calculations are made using the Direct(5,6) method in the two variants which appear in Section 3.2.2. First, we consider spectral solutions for waves of constant form and compare the Fourier–Boussinesq approximation with the exact equations. From this we find that the method, when combined with a five-term Taylor series expansion from $z = 0$ to $z = \eta$, achieves high accuracy for waves very near the stable limiting steepness at any $\kappa$. When the free-surface perturbation scheme is adopted however (allowing direct matrix methods to be used) the model is found to break down at approximately 80% of the limiting steepness for all $\kappa$. Next, a finite-difference–FFT implementation is discussed for treating more general problems. This code is applied to several test cases including: linear shoaling over a smooth beach; Bragg reflection from a rippled bottom; harmonic generation by waves passing over a submerged bar; and nonlinear shoaling of an irregular wave spectrum from deep to shallow water.

### 5.1. A spectral solution for highly nonlinear steady waves on a flat bottom

As shown by [28], steady solutions to the exact Laplace problem right up to the steepest wave, can be computed with great accuracy using a spectral method based on the stream function. Here we apply the same technique to solve the Fourier–Boussinesq Direct(5,6) approximation, and compare to the exact equations. In order to treat the very long wave limit, an expansion in terms of Jacobian elliptic functions would be more rapidly convergent as shown by [29], but we avoid approaching this limit here.

Boussinesq approximations typically begin with a Taylor expansion of the velocity potential however, in two-dimensions we may just as well use the stream function. Using the notation of Taylor operators, an analogous expression to (9) in a frame of reference moving at the wave celerity $c$ is

$$\psi(x,z,t) = \bar{u}(h+z) + \cos(z\nabla)\hat{\psi} + \frac{\sin(z\nabla)}{\nabla}\hat{u}, \tag{49}$$

where $\hat{\psi} = \psi(x,0)$ (and in two-dimensions $\nabla$ is just $\partial/\partial x$). Thus, all surface quantities can be expressed in terms of the $z = 0$ quantities through

$$\begin{aligned} &\tilde{\psi} = \bar{u}(h+\eta) + \cos(\eta\nabla)\hat{\psi} + \frac{\sin(\eta\nabla)}{\nabla}\hat{u}, \\ &\tilde{u} = \bar{u} + \cos(\eta\nabla)\hat{u} + \sin(\eta\nabla)\widehat{w}, \qquad \widetilde{w} = -\sin(\eta\nabla)\hat{u} + \cos(\eta\nabla)\widehat{w}, \end{aligned} \tag{50}$$

while $\hat{u}$ and $\widehat{w}$ are related via the bottom boundary condition (12).

To get a numerical solution, the sine and cosine operators in (50) are truncated, while the tangent operator in (12) is replaced by a rational approximation. We note that Truncation of the Taylor operators at order $M$ is similar to using $M$ steps in the explicit free-surface perturbation procedure, but performs better for very steep waves as discussed in Section 5.1.1. Now, $\hat{\psi}$, $\hat{u}$, and $\widehat{w}$ are expanded in Fourier series as

$$\hat{\psi} = \sum_{j=1}^{n} \frac{C_j}{jk}\cos(jkx), \qquad \hat{u} = \sum_{j=1}^{n} B_j \cos(jkx), \qquad \widehat{w} = \sum_{j=1}^{n} C_j \sin(jkx). \tag{51}$$

This reduces the bottom condition to an algebraic relationship between the coefficients: $C_j = \tanh(jkh)B_j$, where the hyperbolic tangent is replaced by the appropriate rational approximation. Using (50), (12), and (51) in the free-surface conditions at $n+1$ equally spaced points from wave crest to wave trough gives $2n+2$ equations. These equations, together with the kinematic constraints are then solved using Newton's method, as in [28].

Table 3 and Fig. 5 show the wave conditions chosen for calculation, along with a rational fit (Eq. (32) from [30]) to the experimental data of Williams [31], which provides a convenient reference for the steepest stable wave. (For the theory of the highest stable wave, see e.g. [32–35].) Note that each test condition represents a wave of something close to 90% of the limiting steepness ($H$, $L$, and $h$ are the wave height, wave length, and water depth respectively.) In all cases except for $\kappa = 0.2$, $n = 24$ modes was enough to ensure that $B_n/B_1 \leqslant 10^{-9}$ for both the exact and the approximate equations. For the extreme shallow water case with $\kappa = 0.2$ (practically a solitary wave) more modes were required and $n = 40$ gave $B_n/B_1 \approx 10^{-5}$ which was judged to be sufficiently accurate. As noted by [28] and others, very steep waves require sub-steps in wave height in order to

Table 3
Steady nonlinear wave conditions chosen for comparison between spectral solutions of the Fourier–Boussinesq Direct(5,6) and the exact equations. $H$, $L$, and $h$ are wave height, wave length, and water depth

| $\kappa$ | 0.2 | 0.5 | 1 | 2 | 3 | 5 | 10 | 20 | 25 | 30 | 40 | 50 | 100 |
|---|---|---|---|---|---|---|---|---|---|---|---|---|---|
| $H/L$ | 0.02 | 0.045 | 0.09 | 0.11 | 0.12 | 0.13 | 0.13 | 0.13 | 0.13 | 0.13 | 0.13 | 0.13 | 0.13 |
| $H/h$ | 0.65 | 0.565 | 0.565 | 0.36 | 0.26 | 0.16 | 0.08 | 0.04 | 0.033 | 0.027 | 0.02 | 0.016 | 0.008 |

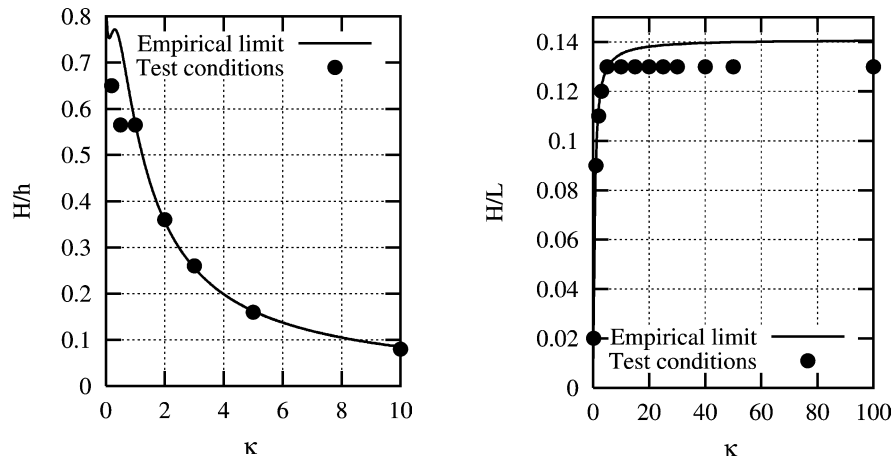


Fig. 5. Test matrix from Table 3 relative to empirical data for the steepest stable wave.

avoid multiply peaked solutions. This is especially true in very shallow water where the extremely narrow peak requires many modes for accurate resolution. Fig. 6 plots the errors in nonlinear dispersion (wave celerity), integrated surface profile, and integrated surface velocity; as functions of $\kappa$ for these highly nonlinear waves. The Taylor operators in (50) are truncated at $M = 5$ for these calculations and the error metrics used are

$$e_c = \frac{c^{\mathrm{e}} - c}{c^{\mathrm{e}}}, \qquad e_\eta = \frac{2}{HL}\left(\int_0^L (\eta^{\mathrm{e}} - \eta)^2 \,\mathrm{d}x\right)^{1/2},$$
$$e_u = \frac{2}{\tilde{u}^{\mathrm{e}}_{\max} L}\left(\int_0^L (\tilde{u}^{\mathrm{e}} - \tilde{u})^2 \,\mathrm{d}x\right)^{1/2}, \qquad e_w = \frac{2}{\tilde{w}^{\mathrm{e}}_{\max} L}\left(\int_0^L (\tilde{w}^{\mathrm{e}} - \tilde{w})^2 \,\mathrm{d}x\right)^{1/2}, \tag{52}$$

where the superscript e indicates the computed value using the exact equations.

These calculations represent the ideal behavior of a general numerical solution to the method in implicit form, i.e. the Direct(5,6) approximation combined with a five-term truncated Taylor series expansion and solved iteratively, as illustrated in Section 3.1. In this case we find that the fully dispersive behavior of the method carries over to steady highly nonlinear waves on a flat bottom; with errors of the same order of magnitude, and following the same trend as was found for linear quantities.

*5.1.1. Limitations associated with the free-surface perturbation procedure*

In order to apply direct methods for solving the discrete linear system of equations obtained from the model, we replace the truncated Taylor series expansion of (50) with the free-surface perturbation procedure of (5), (6), and (7). To investigate the limitations associated with solving in this manner, we consider the steady wave solutions discussed above using the following procedure:

(1) The spectral solution to the exact equations is used to give $n$ equally spaced values of $\eta$ and $\tilde{\phi}$ from wave crest to wave trough. This gives $\hat{\phi}^{(1)}$ from (6).
(2) $\partial^n \hat{\phi}^{(1)}/\partial z^n$ is computed spectrally by the operation $\mathcal{F}^{-1}\{k^n \tanh(\kappa)\mathcal{F}\{\hat{\phi}^{(1)}\}\}$ for $n$ odd and $\mathcal{F}^{-1}\{k^n \mathcal{F}\{\hat{\phi}^{(1)}\}\}$ for $n$ even. Using $\tanh(\kappa)$ here represents the original method of [18], while the Direct(5,6) method is obtained by replacing $\tanh(\kappa)$ with (20) and the coefficients of (19).
(3) $\hat{\phi}^{(2)}$ is computed from (7).

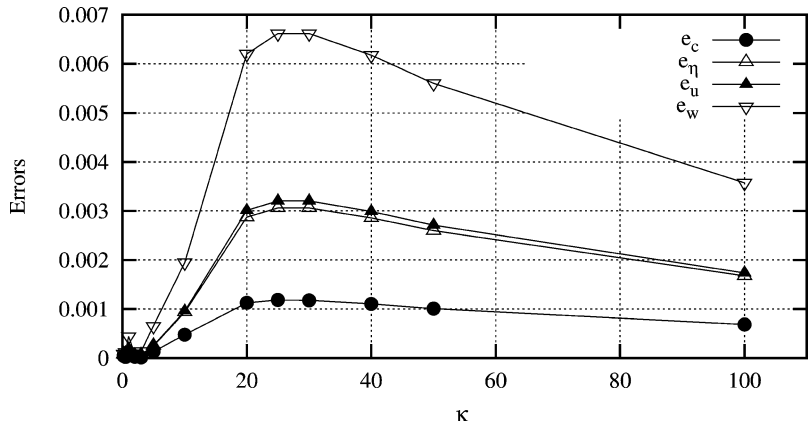


Fig. 6. Errors in nonlinear dispersion, and integrated surface profile and velocity computed using spectral solutions of the Fourier–Boussinesq Direct(5,6) and the exact equations. See (52) for definition of the error metrics.

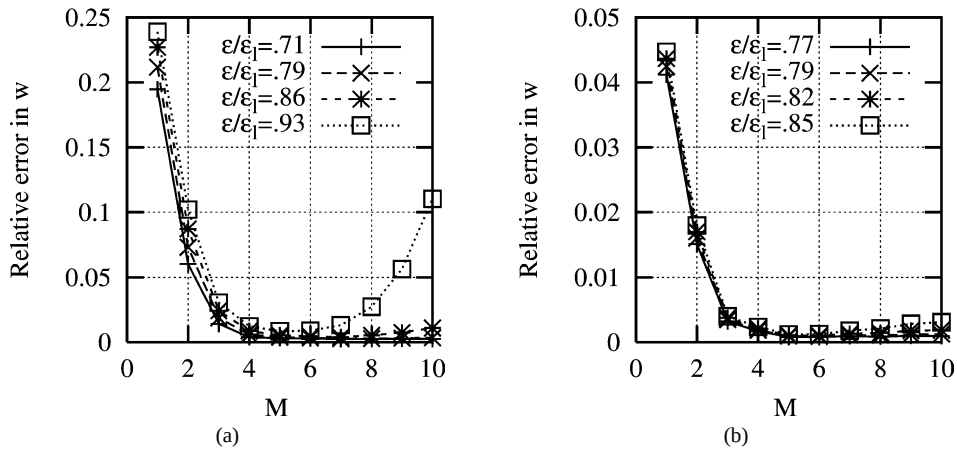


Fig. 7. Two examples of convergence with $M$ for the relative error in $\widetilde{w}$ using the Direct(5,6) method combined with the perturbation procedure of (5)–(7) for nonlinear steady waves approaching the stable limit. (a) $\kappa = 100$, $\epsilon_l = H/L = 0.14$, (b) $\kappa = 0.2$, $\epsilon_l = H/h = 0.75$. $H$, $L$, and $h$ are wave height, wave length, and water depth.

(4) Steps 2 and 3 are repeated to compute the remaining $\hat{\phi}^{(m)}$, $m = 3, 4, \ldots, M$, and their $z$-derivatives.
(5) $\widetilde{w}$ is computed from the $z$-derivative of (5).

Fig. 7 shows two examples of the convergence of the scheme at several values of wave steepness approaching the stable limit for a deep water ($\kappa = 100$) and a shallow water ($\kappa = 0.2$) case. In both cases we see that the scheme begins to diverge for increasing $M$ at a steepness of approximately 80% of the stable limit. This trend is observed for all the values of $\kappa$ represented in Table 3. For these examples we have used $n = 64$ and $n = 128$ respectively, and while increasing the resolution also improves the saturation accuracy of the calculations for conditions below the convergence limit, it does not change the trend that conditions above this limit diverge.

These calculations show that a general numerical solution of the method in direct form is still fully-dispersive, but suggest that it will break down for waves higher than approximately 80% of the stable limiting steepness. This conclusion is confirmed by the calculations of Section 5.2.1. We note that even though it might be inferred from Fig. 7 that simply fixing $M = 4$ or 5 would allow even steeper waves to be treated, we find in practice that the solution quickly becomes unstable for waves significantly above this limit.

### *5.2. A finite-difference–FFT solution for variable depth problems*

In order to treat more general problems, a finite-difference–FFT solution of the Fourier–Boussinesq Direct(5,6) method, in the two variants derived in Section 3.2.2, was developed. The two variants are: the augmented mild-slope form of (34), (35)

and (39); and the mild-slope version of this form where (39) is replaced by (43) and the coefficients of Table 2. We provide here an outline of the solution procedure, and present calculations in one horizontal dimension, while a more detailed description of the numerical issues involved and calculations in two horizontal dimensions will appear in future publications.

The solution is computed on an evenly spaced grid of points at the still water level. Continuous derivatives up to the sixth are replaced by centered finite-difference schemes using at least seven points. All derivatives make use of the entire stencil producing more accuracy for lower derivatives than higher ones, which we have found to be advantageous. No-flux boundary conditions corresponding to a wall are applied at the horizontal boundaries by reflecting the finite-difference coefficients in a symmetric way for $\eta$ and $\widehat{w}$ and an anti-symmetric way for $\hat{\mathbf{u}}$. Non-periodic conditions, and/or wave generation and absorption, are implemented using the methods discussed in Section 4. The time integration of the free-surface conditions is performed using the fifth-order Cash–Karp–Runge–Kutta method which provides an estimate of the error.

In mild-slope form, the continuous derivatives appearing in (35) and (43) are replaced by finite difference approximations, and the equations are enforced at the grid points to obtain the two sparse linear systems of equations

$$\mathbf{B}_0\widehat{w}_0 = \mathbf{A}_{01}\hat{\mathbf{u}} + \mathbf{A}_{02}\mathcal{H}\nabla\hat{\mathbf{u}}, \tag{53}$$

$$\mathbf{B}_1\widehat{w}_1 = \mathbf{A}_{11}\hat{\mathbf{u}}. \tag{54}$$

Having solved for $\widehat{w}_0$ and $\widehat{w}_1$, the total vertical velocity is $\widehat{w} = \widehat{w}_0 + \widehat{w}_1$. These linear systems must be solved once at each level of nonlinearity in the free-surface perturbation procedure, during every stage of the time integration. The finite-difference matrices $\mathbf{B}_0$, $\mathbf{A}_{01}$, $\mathbf{A}_{02}$, $\mathbf{B}_1$, and $\mathbf{A}_{11}$ are banded in one horizontal dimension and sparse in two horizontal dimensions. The number of non-zero elements in each of these matrices is approximately the stencil size times $N$. The Hilbert transform $\mathcal{H}\nabla$ is evaluated using two fast sine transforms (either one or two dimensional) which is appropriate for wall conditions at the horizontal boundaries. Since the matrices are time-independent, and in one horizontal dimension banded, it is advantageous to factor $\mathbf{B_0}$ and $\mathbf{B_1}$ once and for all, and then back-substitute for subsequent solutions. For large problems in two horizontal dimensions however, it may be faster to solve using an iterative technique. The scheme is generally stable, but high-frequency oscillations do tend to appear near the peaks of very steep waves, especially near discontinuities in the depth. When this occurs we apply Savitsky–Golay smoothing at the finite-difference stencil size. The solution effort in one horizontal dimension is thus of the order $MN\log N$ for every stage of the time integration for $M$ steps in nonlinearity.

In augmented mild-slope form, we write $\widehat{w}_1 = \widehat{w}_{11} + \widehat{w}_{12}$ where

$$\widehat{w}_{11} = \sec(h\nabla)\nabla\big(\delta\sec(h\nabla)\nabla\hat{\phi}\big), \qquad \widehat{w}_{12} = B_0^{-1}(\delta B'\nabla\widehat{w}_0 + \delta A'\nabla\cdot\hat{\mathbf{u}}). \tag{55}$$

Discretizing the Padé (4,6) approximation of $\sec(h\nabla)$ in (41), and applying the relation in (40) means solving six linear systems instead of two at each solution step.

*5.2.1. Steep periodic waves of constant form*

The calculations in Section 5.1.1 suggest that the Direct(5,6) method discussed above should be able to treat steady, periodic nonlinear waves up to approximately 80% of the stable limiting steepness, for any $\kappa$. This section summarizes a series of calculations which confirm that this is the case in practice. For this test case we use the semi-analytic solutions discussed in Section 5.1 as initial and boundary conditions for the numerical model. The wave is generated in a relaxation zone two wavelengths long at one end of the domain and absorbed by another of the same length at the other end. The wave travels freely in the domain for five wavelengths, and each simulation is run for ten wave periods after a steady state has been reached. The final free-surface profile in the free part of the domain is then compared to the analytic result to get a measure of the overall error due to all sources for realistic applications of the model. The results are summarized in Table 4, where the integrated error $e_\eta$ is defined in (52), with $\eta^{\mathrm{e}}$ the computed value from stream-function theory. In each case the wavelength was chosen to be one, so that $L = 5$, while $H$ and $h$ were varied to produce the conditions shown in the table, $M = 4$ terms were included in the free-surface perturbation scheme. Each case is at approximately 80% of the limiting steepness for a stable wave at that value of $\kappa$. For all cases other than $\kappa = 0.2$, 32 points per wavelength and 100 points per wave period were used. The $\kappa = 0.2$ case, being essentially a solitary wave of $H/h = 0.57$, required 128 points per wavelength and 800 points per period to obtain this level of accuracy. Calculations consistently broke down for waves significantly steeper than 80% of the maximum.

*5.2.2. Linear shoaling*

We next consider the linear shoaling properties of the model, and verify that the two variants discussed above, converge to the same result when reflection and higher derivatives of $h$ are negligible. (When solving linear problems the nonlinear terms in the free-surface boundary condition are switched off and $M = 1$ is used in the free-surface perturbation procedure.) We use an infinitely smooth bathymetry defined by

$$h(x) = h_0 - \frac{h_0 - h_1}{2}\left[1 + \tanh\left(\frac{\sin(\pi x/l)}{1-(2x/l)^2}\right)\right], \quad -\frac{l}{2} \leqslant x \leqslant \frac{l}{2}; \tag{56}$$

Table 4
Steady nonlinear wave conditions used to evaluate the practical errors incurred by the Fourier–Boussinesq Direct(5,6) method. The error $e_\eta$ is defined in (52)

| $\kappa$ | 0.2 | 1 | $2\pi$ | 100 |
|---|---|---|---|---|
| $H/L$ | 0.018 | 0.075 | 0.11 | 0.11 |
| $H/h$ | 0.566 | 0.47 | 0.11 | 0.0069 |
| Error $e_\eta$ | 0.045 | 0.04 | 0.045 | 0.03 |

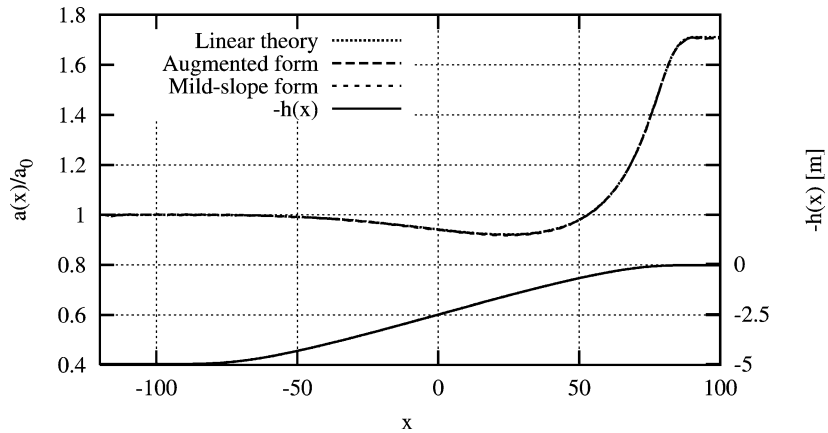


Fig. 8. Amplitude envelope of a linear wave shoaling up a smooth beach. Calculations using the Direct(5,6) method in the augmented mild-slope form of (39), and the mild-slope form of (43).

with $h_0 = 5$, $h_1 = 0.05$, and $l = 256$ (see Fig. 8). This gives $h_x \leqslant 0.04$, with each higher derivative an order of magnitude smaller than the previous. A linear wave of $L = 10$ is generated at the left end of the domain and allowed to propagate until a steady state has been reached everywhere. This produces relative conditions from deep to shallow water, corresponding to $0.07 \leqslant kh \leqslant \pi$, or approximately a factor of 50 change in the local value of $kh$. A relaxation zone at the left end of the computational domain generates the wave, while one at the right end absorbs it, ensuring minimal reflection from that boundary. The time and space discretizations are refined until convergence to approximately three significant digits is reached using each variant of the method. Fig. 8 shows the amplitude envelope of the converged steady-state time signals, along with that predicted by energy conservation,

$$\frac{a(x)}{a_0} = \left( \frac{k(x)(1 + 2k_0h_0/\sinh(2k_0h_0))}{k_0(1 + 2k(x)h(x)/\sinh(2k(x)h(x)))} \right)^{1/2}. \tag{57}$$

The two variants are seen to converge to the analytic value when higher derivatives of $h$ and reflection are negligible.

*5.2.3. Bragg reflection*

As an example where the form of the variable bottom term does matter, we next consider Bragg reflection from a sinusoidal bottom ripple patch. The conditions of [36] are used, in order to compare with these experiments. The bottom is defined by $h + d\sin(k_b x)$; $-l_0 \leqslant x \leqslant l_0$, and $h$ elsewhere, where $h$ and $d$ are constants. The bottom slope is $k_b d = 0.31$ and $l_0/l_b = 10$ ($k_b = 2\pi/l_b$). The incident wave is at the linear resonance condition of $k = k_b/2$ with a wave steepness of $kH/2 = 0.05$. The time and space discretizations, as well as the nonlinearity $M$ are refined until convergence to approximately 3 significant digits is reached for the steady-state elevation using each variant of the Direct(5,6) method. For this mildly nonlinear case $M = 2$ was sufficient. The local reflection coefficient is then extracted from these time-series using the method of [37] as extended by [4]. The results appear in Fig. 9 for the two cases of $d/h = 0.14$ and $d/h = 0.1$, along with the experimental measurements of [36]. The linear perturbation solution of [38] is also included with the mild-slope calculations. The importance of the higher derivative terms is quite clear from these figures.

Fig. 10 shows the reflection coefficient computed at a number of points near the linearized resonance condition of $2k/k_b = 1$, using a wave steepness of $kH/2 = 0.05$ and a bottom ripple steepness of $k_b d = 0.16$. We note that these results are very similar to those obtained by [4] using a high-order spectral method, and they show the characteristic down-shift of the resonant peak relative to the linear value which is also observed in the experiments.

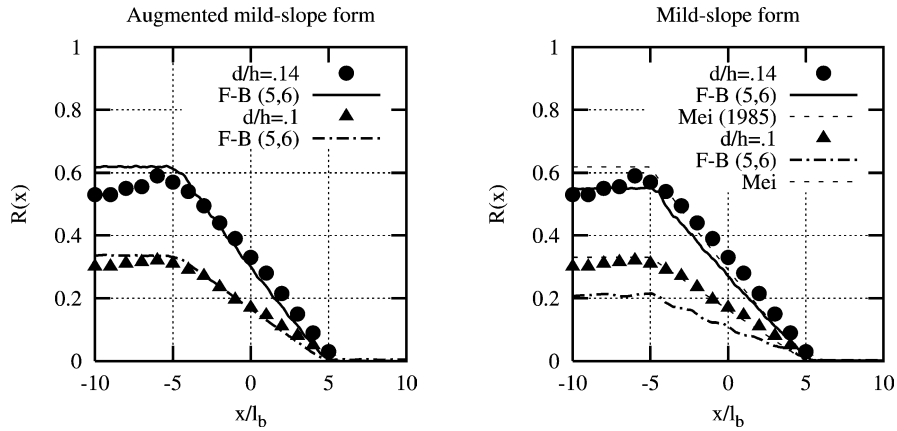


Fig. 9. Bragg reflection from a sinusoidal bottom ripple patch over $-5l_b < x < 5l_b$ with $kH/2 = 0.05$, and $k_b d = 0.31$. Calculations using the Direct(5,6) method in the augmented mild-slope form of (39), and the mild-slope form of (42). Symbols are the measurements of [36]. The linear perturbation theory of [38] is also shown with the mild-slope results.

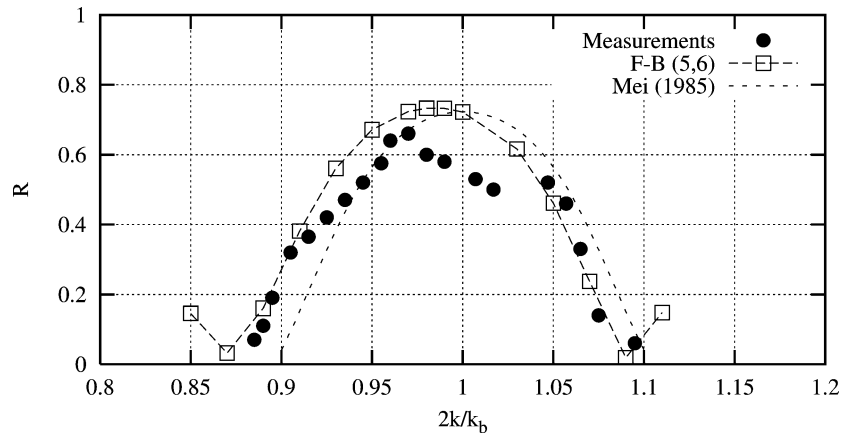


Fig. 10. Bragg reflection coefficient near the linearized resonance condition $2k/k_b = 1$, for $kH/2 = 0.05$, $k_b d = 0.16$. Calculations using the Direct(5,6) method in augmented mild-slope form (39), are compared to the measurements of [36], and the linear perturbation theory of [38].

*5.2.4. Harmonic generation over a submerged bar*

This example considers the transformation of a mildly-nonlinear, monochromatic wave as it travels up and over a submerged bar. As the wave shoals up the front face of the bar it steepens dramatically, accumulating higher harmonics which are released on the downslope producing an irregular pattern behind the bar. This phenomenon is often used as a strenuous test case for nonlinear models of surface wave propagation on a variable bottom. Many authors have considered the problem, both experimentally (e.g. [39] and [40,41]), and numerically (e.g. [42,43], and [9]). The geometry of the experiment can be found in [40], and is usually scaled by a factor of two, to make it equivalent to [39].

Fig. 11 compares a portion of the time series at four of the experimental measurement points. The left column shows the long wave ($T = 2.01$ s) case, and the right column the short wave ($T = 1.01$ s) case. Computations for both cases have been made on both a coarse and a fine grid to ensure convergence. The coarse grid used 1025 grid points over $0 \leqslant x \leqslant 30$, and 2001 time steps for $0 \leqslant t/T \leqslant 50$; while the fine grid used twice as many points in both time and space. $M = 4$ steps in nonlinearity were taken in both cases. Additional runs were also made using $M = 6$, and twice as many time steps, producing insignificant changes to the results. Only the fine grid results are shown in the figures as the coarse grid calculations are indistinguishable at this scale. The comparison is reasonably good, and similar to results obtained using other fully (or highly) dispersive methods.

*5.2.5. Shoaling irregular waves – an engineering application*

We close with an example of an engineering application for which this method is particularly well suited: the deterministic prediction of wave climate in the near shore region given generic deep water conditions offshore. This is a tool which is of interest to engineers involved in building coastal wind-power plants for example. Such installations are often put in water

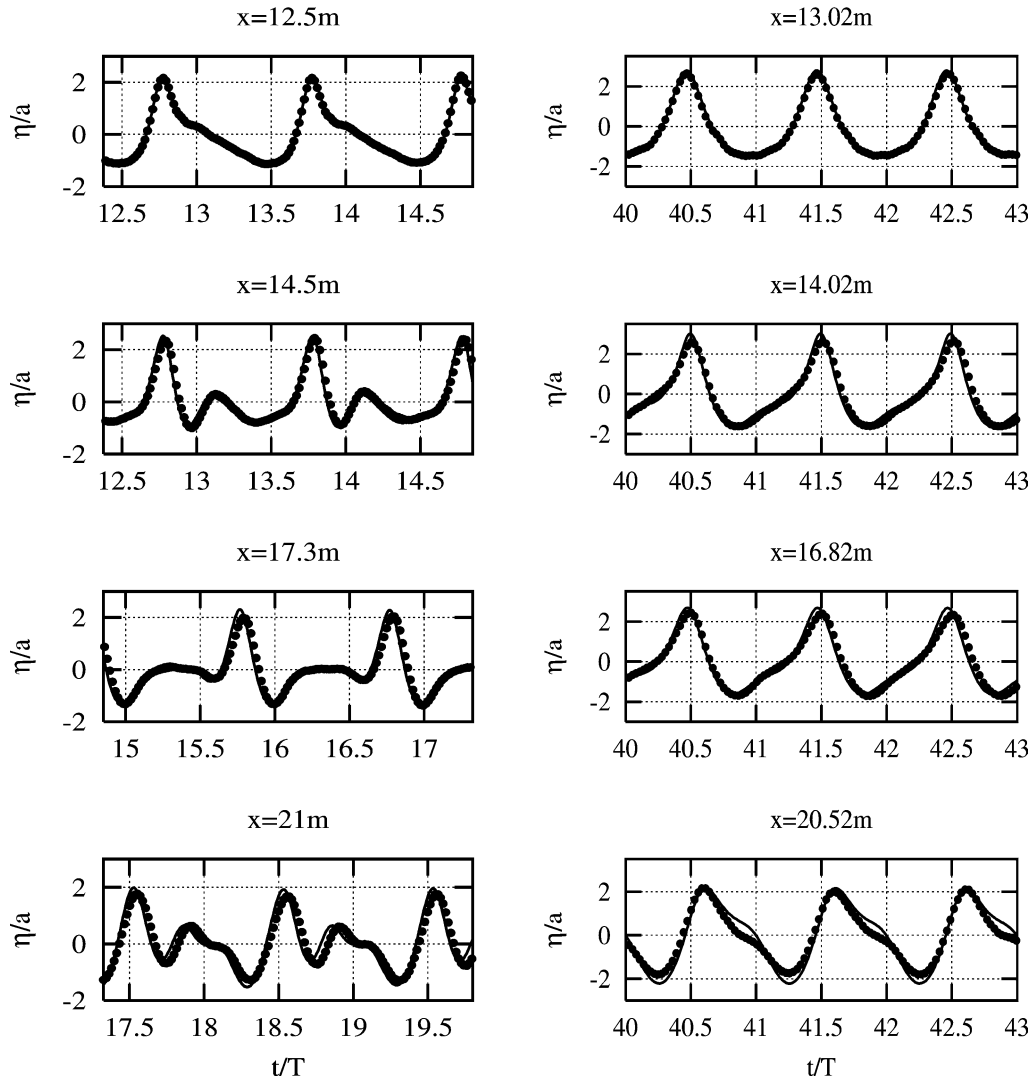


Fig. 11. Time series of measured and computed surface elevations at four positions for waves passing over a bar. The solid line shows the calculations and the points are the measurements. Left: long wave case from [40], $T = 2.01$ s, $a = 0.02$ m. Right: short wave case from [41], $T = 1.01$ s, $a = 0.0405$ m.

depths of around 10 m in countries which border the North Sea. Fig. 12 shows the square root of the spectral density (which is proportional to wave height) for a typical North Sea JONSWAP spectrum plotted against cyclic frequency $f$. The peak period is $T_p = 12$ s and the significant wave height $H_s = 7.5$ m. If the peak wave of this spectrum is placed at the approximate deep water limit of $kh = \pi$, then the offshore water depth should be $h_0 = 120$ m. To include all short wave energy in the analysis with wave heights larger than 5% of the peak wave height, we get a short wave cut-off frequency of approximately 0.28 which corresponds to $k_{\max} h_0 = 37$ at the offshore limit of the domain. This simple example illustrates the need to simultaneously consider both a large variation in $h$ and large variation in $k$ and represents a difficult challenge for most nonlinear wave models.

The spectrum discussed above was used to generate a pseudo-random time series as boundary conditions at the left end of a 7 km long domain where the depth decreases from $h_0 = 120$ m to $h_1 = 10$ m at an average slope of around 2% using (56). The simulation was run for approximately 55 minutes of real time corresponding to $2^{15}$ time steps at $dt = 0.1$ s with $N = 2^{11}$ grid points over the domain and $M = 3$ steps in nonlinearity. This required approximately 18 minutes of CPU time on a 2.26 MHz Pentium IV machine. Fig. 13 shows a snapshot of the free-surface during a particularly large event near the shallow end of the domain, along with the bottom bathymetry. An expanded view of the large wave near the shallow end is shown in Fig. 14 where we can observe its highly nonlinear and asymmetrical features.

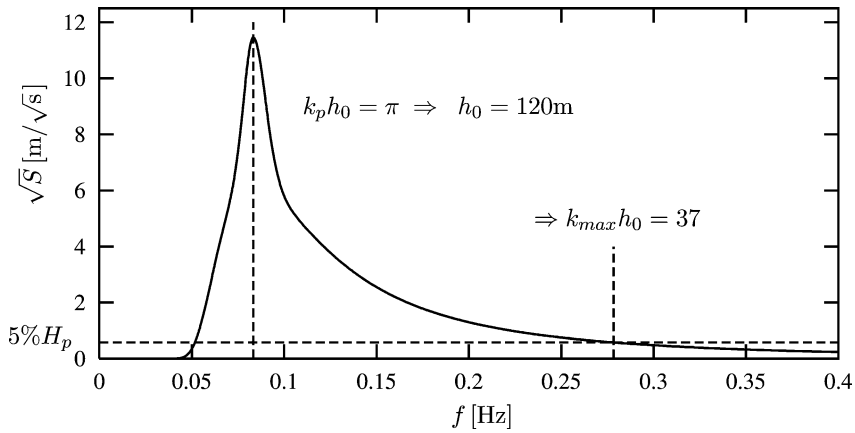


Fig. 12. A typical North Sea JONSWAP spectrum with $T_p = 12$ s and $H_s = 7.5$ m, indicating the range of $kh$ required to shoal these waves from deep to shallow water.

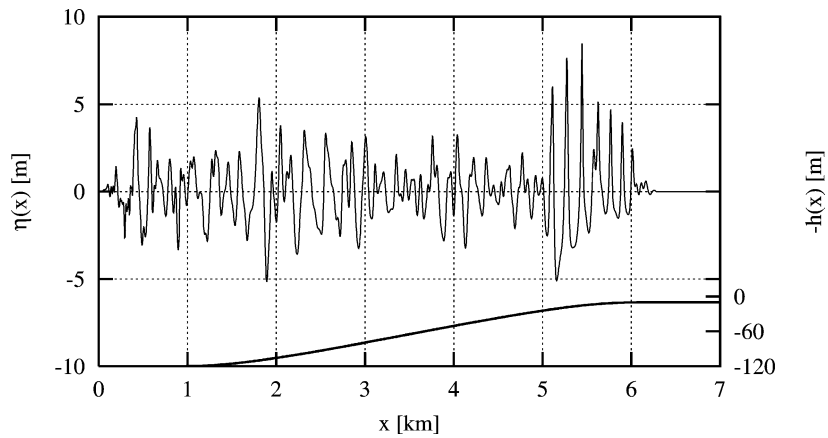


Fig. 13. A snapshot of the free-surface elevation along with the bottom bathymetry for the nonlinear shoaling calculation.

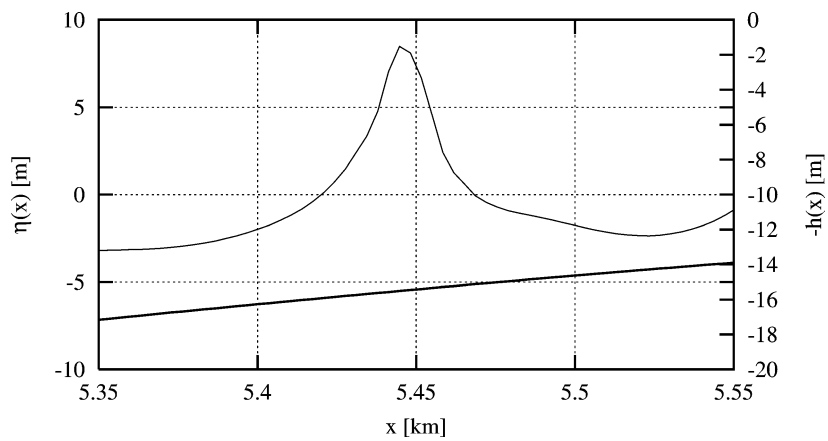


Fig. 14. Expanded view of Fig. 13 around the large shallow water event.

The next step will be to validate such calculations against experimental measurements, after which we intend to use them to help predict the wave loading on near-shore structures.

## References


[1] S.T. Grilli, P. Guyenne, F. Dias, A fully non-linear model for three-dimensional overturning waves over an arbitrary bottom, Int. J. Numer. Methods Fluids 35 (2001) 829–867.
[2] P. Wang, Y. Yao, M.P. Tulin, Wave group evolution, wave deformation, and breaking: simulations using LONGTANK, a numerical wave tank, Int. J. Offshore and Polar Eng. 4 (3) (1998) 200–205.
[3] D. Kring, T. Korsmeyer, J. Singer, J. White, Analyzing mobile offshore bases using accelerated boundary-element methods, Marine Structures 13 (2000) 301–313.
[4] Y. Liu, D.K.P. Yue, On generalized Bragg scattering of surface waves by bottom ripples, J. Fluid Mech. 356 (1998) 297–326.
[5] R.A. Smith, An operator expansion formalism for nonlinear surface waves over variable depth, J. Fluid Mech. 363 (1998) 333–347.
[6] W. Craig, C. Sulem, Numerical simulation of gravity waves, J. Comput. Phys. 108 (1993) 73–83.
[7] W.J.D. Bateman, C. Swan, P.H. Taylor, On the efficient numerical simulation of directionally spread surface water waves, J. Comput. Phys. 174 (1993) 277–305.
[8] D. Clamond, J. Grue, A fast method for fully nonlinear water-wave computations, J. Fluid Mech. 447 (2001) 337–355.
[9] P.A. Madsen, H.A. Schäffer, A review of Boussinesq-type formulations for gravity waves, in: P.L.-F. Liu (Ed.), Advances in Coastal and Ocean Engineering, vol. 5, World Scientific, 1999, pp. 1–94.
[10] J.W. Kim, K.J. Bai, W.C. Webster, R.C. Ertekin, A derivation of the Green–Naghdi equations for irrotational flows, J. Eng. Math. 40 (1) (2001) 17–34.
[11] A.B. Kennedy, J.D. Fenton, A fully nonlinear computational method for wave propagation over topography, Coastal Eng. 32 (1998) 137–161.
[12] K. Nadaoka, S. Beji, Y. Nakagawa, A fully dispersive weakly nonlinear model for water waves, Proc. Roy. Soc. London Ser. A 453 (1997) 303–318.
[13] P.A. Madsen, H.B. Bingham, H.A. Schäffer, Boussinesq formulations for fully nonlinear and extremely dispersive waver waves. Derivation and analysis, Proc. Roy. Soc. London Ser. A 459 (2003) 1075–1104.
[14] P.A. Madsen, O.R. Sørensen, A new form of the Boussinesq equations with improved linear dispersion characteristics. Part 2. A slowly varying bathymetry, Coastal Eng. 18 (1992) 183–204.
[15] O. Nwogu, Alternative form of Boussinesq equations for nearshore wave propagation, J. Waterways, Port, Coastal, Ocean Eng., ASCE 119 (1993) 618–638.
[16] Y. Agnon, H.B. Bingham, A non-periodic spectral method with application to nonlinear water waves, Eur. J. Mech. B Fluids 18 (3) (1999) 527–534.
[17] V.E. Zakharov, Stability of periodic waves of finite amplitude on the surface of a deep fluid, J. Appl. Mech. Tech. Phys. 9 (1968) 190–194.
[18] D. Dommermuth, D.K.P. Yue, A high-order spectral method for the study of nonlinear gravity waves, J. Fluid Mech. 184 (1987) 267–288.
[19] D.P. Nicholls, F. Reitich, Analytic continuation of Dirichlet–Neumann operators, Numer. Math. 94 (1) (2003) 107–146.
[20] D.P. Nicholls, F. Reitich, Stability of high-order perturbative methods for the computation of Dirichlet–Neumann operators, J. Comput. Phys. 170 (1) (2001) 276–298.
[21] D.P. Nicholls, F. Reitich, A new approach to analyticity of Dirichlet–Neumann operators, Proc. Roy. Soc. Edinburgh Sect. A 131 (6) (2001) 1411–1433.
[22] Lord Rayleigh, On waves, Philos. Mag. 5 (1) (1876) 257–279.
[23] Y. Agnon, Linear and nonlinear refraction and Bragg scattering of water waves, Part A, Phys. Rev. E 59 (2) (1999) R1319–R1322.
[24] D. Givoli, Non-reflecting boundary conditions, J. Comput. Phys. 94 (1991) 1–29.
[25] J.E. Romate, Absorbing boundary conditions for free surface waves, J. Comput. Phys. 99 (1992) 135–145.
[26] T.G. Jensen, Open boundary conditions in stratified ocean models, J. Marine Systems 16 (1998) 297–322.
[27] J. Larsen, H. Dancy, Open boundaries in short wave simulations – a new approach, Coastal Eng. 7 (1983) 285–297.
[28] J.D. Fenton, The numerical solution of steady water wave problems, Comput. Geosci. 14:3 (1988) 357–368.
[29] J.D. Fenton, A high-order cnoidal wave theory, J. Fluid Mech. 94 (1979) 129–161.
[30] J.D. Fenton, Nonlinear wave theories, in: B. Le Mehaute, D.M. Hanes (Eds.), The Sea, Wiley, 1990, pp. 3–25.
[31] J.M. Williams, Limiting gravity waves in water of finite depth, Philos. Trans. Roy. Soc. London Ser. A 302 (1981) 139–188.
[32] E.D. Cokelet, Steep gravity waves in water of arbitrary uniform depth, Philos. Trans. Roy. Soc. London Ser. A 286 (1977) 183–230.
[33] M.S. Longuet-Higgins, Internal properties of periodic gravity waves of finite amplitude, Proc. Roy. Soc. London Ser. A 342 (1975) 157–174.
[34] M.S. Longuet-Higgins, J.D. Fenton, On the mass, momentum, energy and circulation of a solitary wave. II, Proc. Roy. Soc. London Ser. A 340 (1974) 471–493.
[35] L.W. Schwartz, Computer extension and analytic continuation of Stokes' expansion for gravity waves, J. Fluid Mech. 62 (1974) 553–578.
[36] A.G. Davies, A.D. Heathershaw, Surface wave propagation over sinusoidally varying topography, J. Fluid Mech. 144 (1984) 419–443.
[37] Y. Goda, Y. Suzuki, Estimation of incident and reflected waves in random wave experiments, in: Proc. 15th Conf. on Coastal Eng., Honolulu, Hawaii, 1976, pp. 828–845.
[38] C.C. Mei, Resonant reflection of surface water waves by periodic sand-bars, J. Fluid Mech. 152 (1985) 315–335.

[39] S. Beji, J.A. Battjes, Experimental investigation of wave propagation over a bar, Coastal Eng. 19 (1993) 151–162.
[40] H.R. Luth, B. Klopman, N. Kitou, Projects 13G: Kinematics of waves breaking partially on an offshore bar; LDV measurements for waves with and without a net onshore current, Technical Report H1573, Delft Hydraulics, 1994.
[41] M. Dingemans, Comparison of computations with Boussinesq-like models and laboratory measurements, MAST-G8M note H1684, Delft Hydraulics, World Scientific, 1994, 32 p.
[42] M. Dingemans, Water wave propagation over uneven bottoms, Adv. Ser. Ocean Eng. 13 (1997).
[43] S.T. Mayer, A. Garapon, L.S. Sørensen, A fractional step method for unsteady free-surface flow with applications to nonlinear wave dynamics, Int. J. Numer. Methods Fluids 28 (1998) 293–315.